Catalysis Today 167 (2011) 46–55

Contents lists available at ScienceDirect

Catalysis Today

journal homepage: www.elsevier.com/locate/cattod

Zr-SBA-15 as an efficient acid catalyst for FAME production from crude palm oil

Jose Iglesias [a,*], Juan A. Melero [b], L. Fernando Bautista [b], Gabriel Morales [b], Rebeca Sánchez-Vázquez [b], Maria Teresa Andreola [b], Arantzazu Lizarraga-Fernández [b]

[a] Department of Chemical and Energy Technology, Universidad Rey Juan Carlos, C/ Tulipán s/n, E-28933, Móstoles, Madrid, Spain
[b] Department of Chemical and Environmental Technology, Universidad Rey Juan Carlos, C/ Tulipán s/n, E-28933, Móstoles, Madrid, Spain

ARTICLE INFO

Article history:
Received 21 May 2010
Received in revised form
12 November 2010
Accepted 25 November 2010
Available online 22 December 2010

Keywords:
Biodiesel
Zirconium
SBA-15
Acid catalysis
FAME

ABSTRACT

The synthesis of Zr-SBA-15 materials from zirconocene dichloride as metal precursor has been investigated. These materials can be prepared with a high loading of zirconium while preserving good mesoscopic ordering. Zr-SBA-15 materials display acid properties which have revealed to confer high catalytic activity in the transesterification of crude palm oil with methanol for biodiesel synthesis, achieving yields to FAME over 70% in a batch reactor under the following reaction conditions: 200 °C, 3 h, methanol to oil molar ratio 30:1 and using 10 wt.% catalyst loading referred to oil. Furthermore, Zr-SBA-15 materials display excellent stability in palm oil transesterification, being fully regenerated by calcination at 550 °C after at least eight consecutive reaction runs. The incorporation of titanium, molybdenum and tungsten as doping metals produces slightly promotion of the acidity of Zr-SBA-15 materials, though this is not translated into higher catalytic activity.

1. Introduction

Biodiesel production has become a very intense research area because of the growing interest on finding new resources and alternatives for conventional transport fuels [1]. Nevertheless, the conventional production process, consisting of the use of a homogeneous alkaline catalyst [2] is, at the moment, non-competitive, bearing in mind the low costs associated to the production of conventional fuels [3]. Among many reasons, the cost associated to the feedstock is one of the most important drawbacks in biodiesel production processes [4]. Using homogeneous alkaline catalysts involves the needing of high grade feedstock, like refined oils with low free fatty acid (FFA) content to avoid soap formation by saponification with the catalyst [5]. However, the combination of lower grade feedstock with a pre-treatment step, in which FFA content is reduced by esterification with short chain alcohols, can be used instead [6]. Nevertheless, both alternatives lead to large costs because of the needing of using expensive feedstock or a conditioning stage to pre-treat the raw material. In addition to all these drawbacks, the use of homogeneous catalysts which need to be neutralized after reaction, leads to the contamination of the main biodiesel by-product, the glycerol [6]. In this way, apart from the huge amount of commercially available glycerol which has caused a dramatic reduction of glycerol price during the last years [7], glycerol needs to be purified to be commercialized.

As alternative to the conventional biodiesel production process, the use of heterogeneous acid catalysts has been suggested to be more profitable than conventionally homogeneous alkaline-driven processes [8,9]. However, although acid catalysts are able to drive both FFA esterification and triglycerides transesterification in a single step [10], their catalytic activity in the latter case is substantially lower than that shown by alkaline catalysts. One way to compensate this fact with regards to base catalysts is using strong solid acids with a high concentration of catalytic sites. In this sense, one of the most important industrially applied heterogeneous acid catalysts is the family of zirconium oxide-based materials [11], such as sulfated [12] and tungstated zirconia [13]. These catalysts have proved to be active in numerous acid-driven reactions, including biodiesel production from both the esterification of fatty acids [14–16] and the transesterification of triglycerides [16–19] with short chain alcohols. Nevertheless, several troubles associated to the low stability of promoting species like sulphate ions [20,21], and the very low surface area these materials display [22], limit their application to biodiesel synthesis. The use of mesostructured silica-based supports, which help to enlarge the surface area of zirconium oxide, has proved to be a valuable strategy in many different applications [22–26], though scarcely applied to biodiesel synthesis [27]. Besides, supporting zirconium species onto silica frameworks allow achieving both Lewis and Brønsted acid sites [28] with varying acid strengths depending on the synthesis conditions [29,30]. In this sense, Gracia et al. [31] have recently reported the synthe-

* Corresponding author. Tel.: +34 91 488 8565; fax: +34 91 488 7068.
E-mail address: jose.iglesias@urjc.es (J. Iglesias).

0920-5861/$ – see front matter © 2010 Elsevier B.V. All rights reserved.
doi:10.1016/j.cattod.2010.11.060

sis of a Zr-SBA-15 material through a direct synthesis procedure displaying very highly active Lewis acid species as a result of the interaction of chlorine atoms with zirconium sites, opening new alternatives to metal doped or sulphated zirconias as highly acidic zirconium-based solid catalysts.

Within this contribution, we present the synthesis of Zr-SBA-15 materials, as well as their modification with different doping metals, and their application to biodiesel production from crude palm oil. Both kinds of materials, with and without doping agents, display very high catalytic activity in transesterification reactions without noticeable loss of catalytic activity after thermal regeneration for eight consecutive reaction runs.

2. Experimental

2.1. Materials and methods

Tetraethylorthosilicate (TEOS, Aldrich) and Pluronic P123 (PEO_{20}-PPO_{70}-PEO_{20}, Aldrich) were used as silicon precursor and structure directing agent respectively in the synthesis of SBA-15-type materials. Zirconocene dichloride (Cp_2ZrCl_2, Aldrich), titanocene dichloride (Cp_2TiCl_2, ABCR), ammonium heptamolybdate tetrahydrate ($(NH_4)_6Mo_7O_{24}{\cdot}4H_2O$, Aldrich), tungsten hexachloride (WCl_6, ABCR) and tungstenocene dichloride (Cp_2WCl_2, ABCR) where used as metal sources for the preparation of Zr-SBA-15 and metal-doped related materials. Crude palm oil (FFA content of 5.6 wt.%) and methanol 99% (Scharlab) were used as received in transesterification catalytic assays.

2.2. Materials preparation

2.2.1. Synthesis of Zr-SBA-15 materials

Zr-SBA-15 materials were synthesised according to the method previously described by our group for the synthesis of Ti-SBA-15 materials [32], using zirconocene dichloride as metal precursor. In a typical synthesis, 4 g of pluronic triblock copolymer P123 were dissolved in 125 ml of 0.5N hydrochloric acid at room temperature. After complete dissolution, the proper amount of zirconocene dichloride was added to achieve the desired Si/Zr molar ratio. The suspension was then stirred for 3 h and the final clear solution warmed up at 40 °C. 8.63 g of TEOS were then added in a single step into the synthesis media and the resultant suspension was vigorously stirred for 20 h at 40 °C. The resultant white suspension was hydrothermally aged at 100 °C under static conditions for 24 additional hours. The materials were then recovered by filtration and air-dried overnight. Surfactant was removed from mesoporous channels by calcination in air at 550 °C, using a heating ramp of 1.8 °C min^{-1} and maintaining the final temperature for 5 h under static conditions.

2.2.2. Synthesis of metal-doped Zr-SBA-15 materials

The synthesis of metal-doped zirconium-containing SBA-15 mesostructured materials was accomplished by using a similar procedure to that previously described for Zr-SBA-15 materials except for the addition of the doping agent into the synthesis gel together with the zirconium source. Thus, titanium, molybdenum and tungsten were used as metal sources for doping the zirconium-based materials. The amount of doping agent was varied in a zirconium to doping metal molar ratio range from 1 to 20.

2.3. Materials characterization

N_2 adsorption–desorption isotherms were collected on a Micromeritics TriStar 3000 unit. Surface area values were calculated using the B.E.T. method and pore sizes distribution were achieved through the B.J.H. method assuming cylindrical pore geometry and using a Harkins–Jura type equation specifically fitted for SBA-15 materials [33]. Total pore volume was assumed to be that recorded at $p/p_0 = 0.985$. Bulk metal contents of the synthesized materials were determined by Inductively Coupled Plasma – Atomic Emission Spectroscopy (ICP-AES). Typically, 100 mg of sample were dissolved in aqueous hydrofluoric acid. After dissolution, the sample was transferred to a 250 ml calibrated flask and diluted with water. An absorption standard solution of the corresponding metal (1000 mg/L in water) was used to calibrate the equipment. X-ray powder diffraction patterns (XRD) were collected on a Philips X'pert diffractometer using the CuKα line. The XRD data were recorded in the 2θ range from 0.6° to 5.0° with a step size of 0.02° for low angle analysis and in the 2θ range from 5.0° to 50° using a step size of 0.04° for high angle analysis. Diffuse reflectance UV–vis spectra (DR UV–vis) were recorded under ambient conditions in the wavelength range from 200 to 600 nm. DR UV–vis spectra were collected using a Varian Cary-500. Transmission electron micrographs (TEM) and elemental analysis by EDS (spot beam analysis) were collected in a Philips Tecnai-200 electron microscope operating a 200 kV. Acidity of the samples was determined by ammonia temperature programmed desorption (TPD) in a Micromeritics 2910 (TPD/TPR) equipment. The calcined samples were outgassed under a helium flow (50 N ml min^{-1}) with a heating rate of 15 °C min^{-1} up to 560 °C and kept at this temperature for 30 min. After cooling to 60 °C, an ammonia flow of 35 N ml min^{-1} was passed through the sample for 30 min. The physisorbed ammonia was removed by flowing helium at 60 °C for 90 min. The chemically adsorbed ammonia was determined by increasing the temperature up to 550 °C with a heating rate of 15 °C min^{-1}, maintaining afterwards this temperature for additional 30 min. The ammonia concentration in the effluent stream was measured through a thermal conductivity detector. XPS experiments were carried out in a Specs ultra high vacuum multipurpose surface analysis system operating under 10^{-10} mbar and fitted with a conventional X-ray source (MgKα, 1253.6 eV). Detailed O and Zr high-resolution spectra (pass energy 10 eV, step size 0.1 eV) were recorded at rt using a Phoibos 10-MCD energy analyzer. Prior to their analysis, samples were outgassed at $<10^{-6}$ Torr overnight. Binding energies were referenced to the C1s line (284.6 eV) and deconvolution curves were achieved using the Casa XPS program.

2.4. Catalytic tests

Catalytic reaction runs were driven in a 25 ml stainless-steel autoclave (Autoclave Engineers) fitted with a temperature controller, mechanical stirrer and a pressure transducer for monitoring the reaction conditions. In a typical assay, vegetable oil (5 g), methanol (5.66 g, methanol-to-oil molar ratio of 30) and the catalyst (0.5 g; 10 wt.% referred to oil) were placed inside the reactor and the temperature and stirring conditions (2000 rpm) were set up. The reactions were carried out during 3 h and afterwards the reactor was cooled down using an ice-water bath. The products were recovered from the reactor and mixed with acetone (25 ml), as agent for cleaning the reactor vessel and stirrer. The final solution was then filtered to recover the catalyst before removing the residual methanol and acetone in a rotary evaporator. In the recycling tests, recovered catalysts were double-washed with methanol and n-hexane for the removal of both polar and non-polar surface-adsorbed compounds [34] or calcined in air under static conditions. The calculation of the yield of fatty acid alkyl chains – comprising both FFA and glycerides – towards fatty acid methyl esters (FAME) in the transesterification reactions was carried out on the reaction samples without any further purification. For doing so, ^1H NMR analyses were performed in a Varian Mercury Plus 400 unit in a similar way to that described by Schuchardt [35].

Table 1
Physico-chemical properties of Zr-SBA-15 materials with various metal loadings.

Sample	Zr [a] (wt.%)	η [b] (%)	S_g [c] (m^2/g)	D_p [d] (Å)	V_p [e] (cm^3/g)	$V_{\mu p}$ [f] (cm^3/g)	d_{100} [g] (Å)	a_0 [h] (Å)	W_t [i] (Å)	Acid loading [j] (meq g^{-1})	T_{max} [k] (°C)
S1	5.4 (20)	77	772	104	1.378	0.083	112	129	25	0.17	246
S2	7.3 (15)	80	720	104	1.274	0.066	115	132	28	0.25	259
S3	8.7 (10)	65	632	106	1.182	0.039	118	136	29	0.31	274
S4	11.7 (5)	46	608	99	0.954	0.037	–	–	–	0.23	240

[a] Zirconium content in the final sample measured by ICP-AES Si/Zr molar ratio in synthesis in brackets.
[b] Zirconium incorporation efficiency.
[c] Surface area measured by the B.E.T. method.
[d] Mean pore size calculated through the B.J.H. method.
[e] Total pore volume recorded at $p/p_0 = 0.985$.
[f] Micropore volume calculated through the *t*-plot method according to Ref. [33].
[g] Interplanar spacing calculated through the Bragg's law from XRD experiments.
[h] Unit cell parameter calculated as $a_0 = 2/\sqrt{3}d_{100}$.
[i] Pore wall thickness calculated as $a_0 - D_p$.
[j] Acid loading measured from NH_3 uptake in TPD profiles.
[k] Maximum of the NH_3 TPD curve.

3. Results and discussion

The main aim of this investigation is to prepare Zr-SBA-15 materials showing highly accessible homogeneously dispersed zirconium species which could be used as zirconia-based materials with large area values over which building acid sites by metal doping for the synthesis of biodiesel. With this purpose, the use of zirconocene dichloride, reported for the first time in the present contribution for the synthesis of Zr-SBA-15 materials, allows taking advantage of the hydrophobic nature of cyclopentadienyl rings in the metal source to selectively drive the incorporation of the same in accessible locations, being the same stragety previously described for the synthesis of Ti-SBA-15 [32] and Ti-TLCTS [36] (*True Liquid Crystal Templated Silica*) materials. Thus, the interaction of the zirconium source, during the synthesis step, with the hydrophobic core of the structure directing agent micelles is the responsible factor for the final location of zirconium species on the surface of the mesopores after calcination.

3.1. Synthesis of Zr-SBA-15 materials

In order to determine the effect of the zirconium loading on the properties of final materials, the metal loading into the synthesis gel was varied in the silicon to zirconium molar ratio range from 5 to 20. Table 1 lists the physico-chemical properties achieved for the so-prepared zirconium-containing SBA-15 materials. The analysis of the metal content achieved on the final materials indicates that the incorporation of zirconium species to the silica framework, though high, is not complete. Increasing the metal content in the synthesis media leads to lower incorporation efficiencies, suggesting a possible saturation effect on the ability of micelles to accommodate the metal precursor. Thus, for moderate loadings (samples S1 and S2) the incorporation efficiency is almost 80% of the synthesis values but it decreases to less than 50% for a silicon to zirconium molar ratio of 5 (sample S4).

With regards to the textural properties calculated from nitrogen adsorption isotherms, it seems that the insertion of the zirconium species in large quantities leads to an overall reduction of the surface area and pore volume, whereas mean pore size is slightly modified. This trend is a consequence of the increasing loading of zirconium species inside the mesopores, being responsible of the volume loss detected from adsorption isotherms. These results are clearly evident in Fig. 1, which displays the nitrogen adsorption–desorption isotherms (A) and pore size distributions (B) calculated by the B.J.H. method for the Zr-SBA-15 materials showing varying amounts of metal species. All the samples display

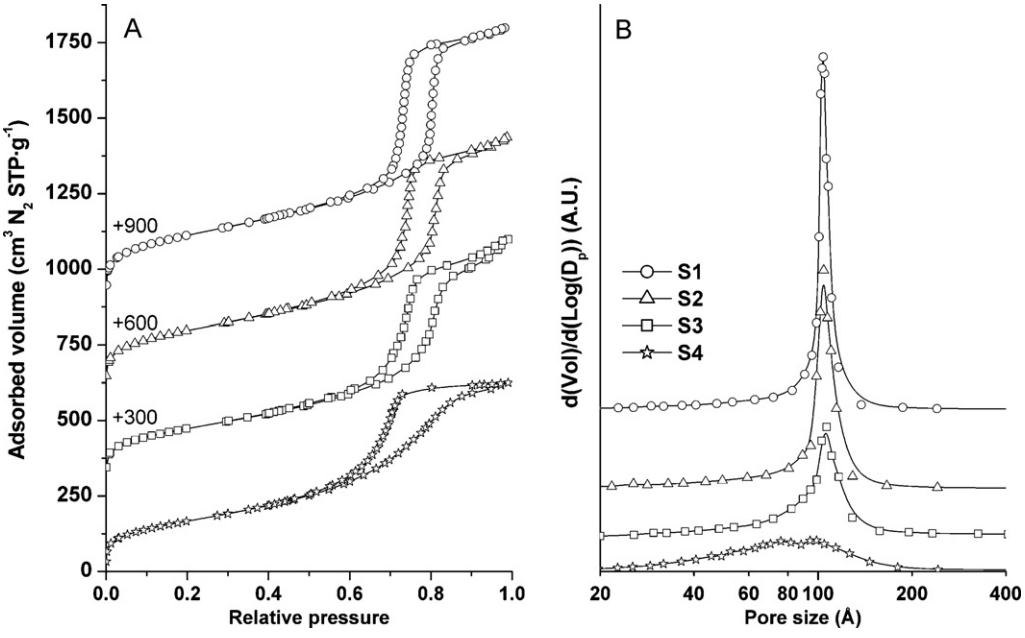

Fig. 1. Nitrogen adsorption–desorption isotherms (A) recorded at 77 K and pore sizes distributions (B) for Zr-SBA-15 materials with different metal loadings.

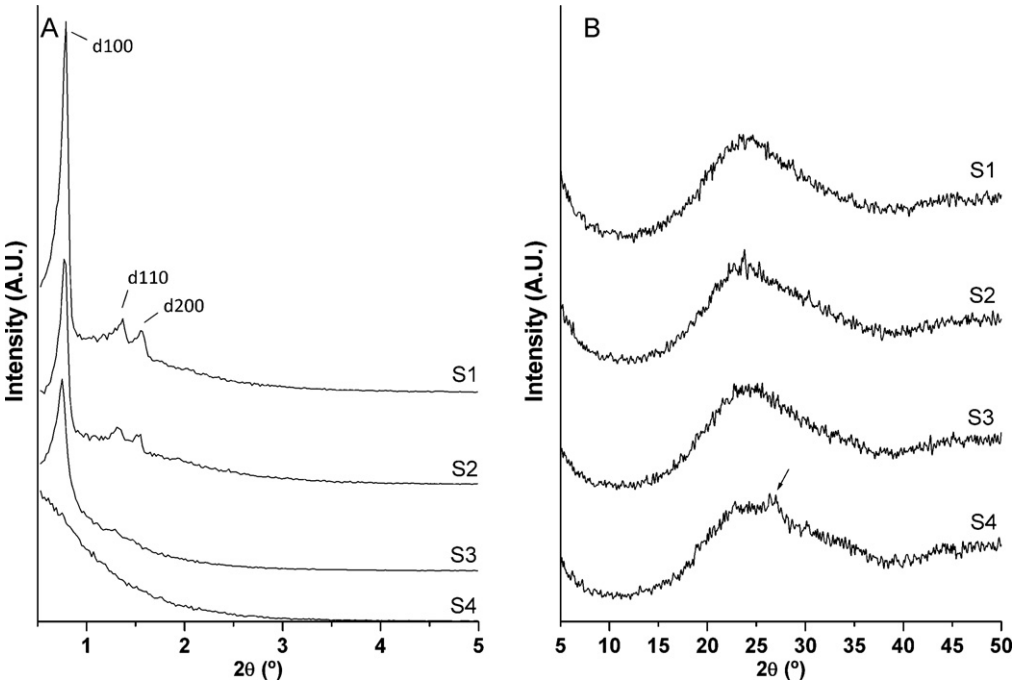

Fig. 2. Zr-SBA-15 X-ray diffraction patterns recorded at (A) low and (B) high angle values.

the typical type IV hysteresis loops corresponding to mesoporous materials, according to the I.U.P.A.C. classification [37], though several important differences are clearly visible between them. Thus, when increasing the zirconium loading, both the total volume reached in the upper plate of the isotherm becomes lower. Moreover, the H1 hysteresis loop typical from mesostructured materials, clearly visible in sample S1, evolves towards a H2-type, typical from non-structured porous glasses and gels, in sample S4. These results point out to the destructuration of the materials insofar as the amount of zirconium is increased into the synthesis gel. These conclusions are better supported by the calculated pore sizes distributions displayed in Fig. 1(B). Thus, unlike sample S4, containing the maximum metal loading among the tested materials, all the materials display narrow pore size distribution typical from mesostructured materials with maxima located in similar values. However, the area below the curve, corresponding to the pore volume, decreases when increasing the metal loading. Nevertheless, when silicon to zirconium molar ratio of 5 is used, the material suffers a complete destructuration, suggesting the existence of a maximal metal loading which can be accommodated within the silica framework before causing the destructuration of the SBA-15 material. On the contrary, this does not explain why the mean pore size remains almost constant for S1–S3 samples, since the incorporation of higher loadings of metal or metal oxide inside the mesoporous channels should lead to a reduction of their size. A possible explanation lays on the swelling effect caused by the dissolution of the zirconium precursor inside the micelles during the synthesis step, in a similar way to that detected when using titanocene dichloride as metal precursor. In this way, the increasing of the size of micelles due to the insertion of the zirconium precursor is compensated by the occupation of some fraction of the mesopore volume by zirconium oxide species. Some evidence of this behaviour could be ascertained from the observed trend in micropore volume detected through the application of the *t*-plot method to the adsorption branch of the isotherm (Table 1). Thus, as the amount of zirconium precursor in the synthesis gel increases, a lower fraction for micropore volume is achieved, indicating that the incorporation of zirconium species onto the final materials could cause the blockage of the micropores. This is a consequence of the arrangement of the zirconium species onto the surface of the mesoscopic channels during the calcination of the as-made samples.

Fig. 2 displays the X-ray diffraction patterns collected for the Zr-SBA-15 materials. Low angle diffraction patterns (Fig. 2(A)) evidence the lack of mesoscopic ordering when reaching silicon to zirconium molar ratio of 5. In fact, the ordering degree, which could be ascertained from the definition of d_{110} and d_{200} diffractions, decreases as the metal content increases. Thus, for sample S1 three distinct diffractions corresponding to d_{100}, d_{110} and d_{200} planar symmetries are clearly visible, but these become less and less intense when increasing the zirconium loading, up to sample S4, where no diffraction signals are detected, indicating that the material does not show any mesoscopic ordering, supporting the above mentioned conclusions about the desestructuration of the material. Unexpectedly, X-ray diffraction analyses did not show signals attributable to the presence of crystalline phases of zirconium dioxide, except for sample S4, where some diffraction can be observed (see the mark inside Fig. 2(B)). Thus, a low intense shoulder at 27° could indicate the presence of small domains of zirconium dioxide, probably crystallized as tetragonal phase – the most common crystalline phase for zirconium dioxide when calcinating at low temperatures. These conclusions are supported by TEM microphotographs depicted in Fig. 3, in which the mesoscopic ordering is clearly visible for samples S1 and S2, synthesized from silicon to zirconium molar ratios of 20 and 15, respectively. In contrast, microphotograph recorded for sample S3 (Si/Zr = 10, Table 1) evidences some damage on the mesostructure, which is completely missed in sample S4. Elemental analysis recorded by spot beam EDX analysis during TEM micrographs evidenced the lack of uniformity in the elemental composition for sample S4, in which some domains were detected with zirconium loadings as high as 60 wt.% corresponding to zirconium dioxide domains. Nevertheless, their size was so small that XRD experiments were not able to detect their presence.

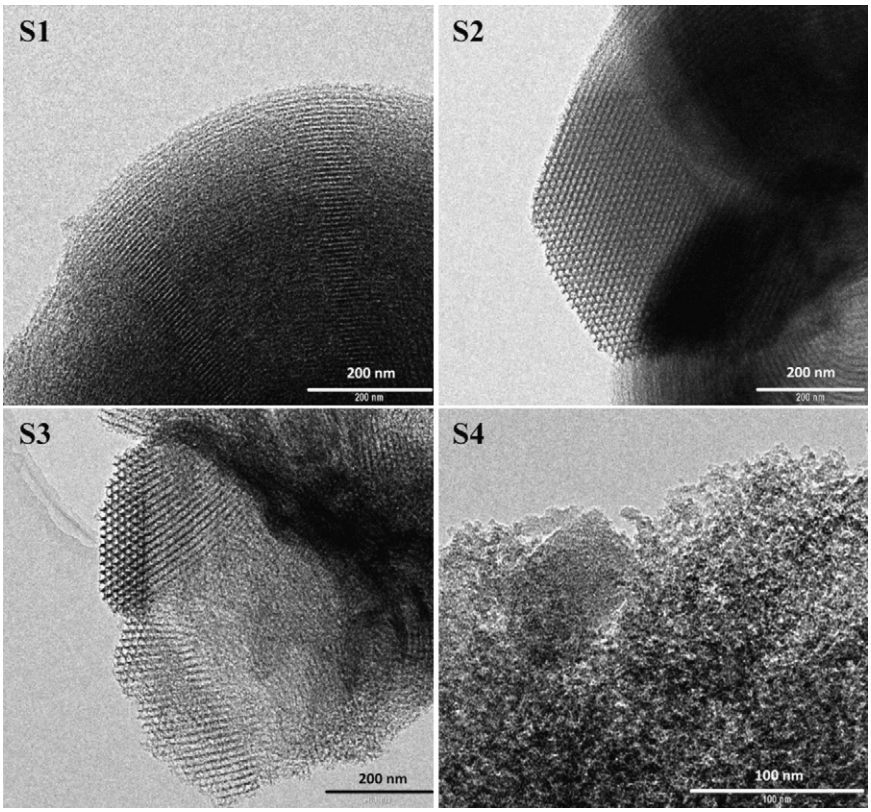

Fig. 3. TEM microphotographs recorded for Zr-SBA-15 materials synthesized with different Si/Zr molar ratios.

With the purpose of getting a better understanding of the nature of the supported zirconium species as well as on their dispersion, DR UV–vis and XPS spectra were recorded for the different Zr-containing materials.

The DR UV–vis spectra of the calcined Zr-SBA-15 materials with different Si/Zr ratios were compared to that obtained for a bulk ZrO_2 sample (Fig. 4). The UV–vis spectra recorded for SBA-15-based materials do not resemble that achieved for bulk zirconia, inferring that Zr supported on SBA-15 samples forms different species. Thus, bulk ZrO_2 displays a very intense and broad band covering 200–245 nm which has been attributed to the overlap of the O→Zr(IV) LMCT (*Ligand to Metal Charge Transfer*) transition and the electron transition from the valence band to the conduction band of ZrO_2 crystallites [38,39]. On the contrary, DR UV–vis spectra recorded for Zr-SBA-15 materials display different absorption bands located at 225, 248 and 290 nm. The first signal has been attributed to the presence of small ZrO_2 clusters since it seems to be caused by the band gap transition in very small ZrO_2 crystallites [39]. On the other hand, signals at 245–290 have been attributed to multicoordinated Zr^{4+} species [25], showing different coordinations, and coming from zirconium dioxide oligomers, dimers and trimers. In this way, it can be concluded that the incorporation of zirconium species onto SBA-15 materials is mainly achieved as oligomers showing Zr–O–Zr bondings. However, increasing the zirconium loading into the synthesis gel produces the formation of zirconium dioxide clusters whose presence is more evident for sample S4, where no mesoscopic ordering is achieved.

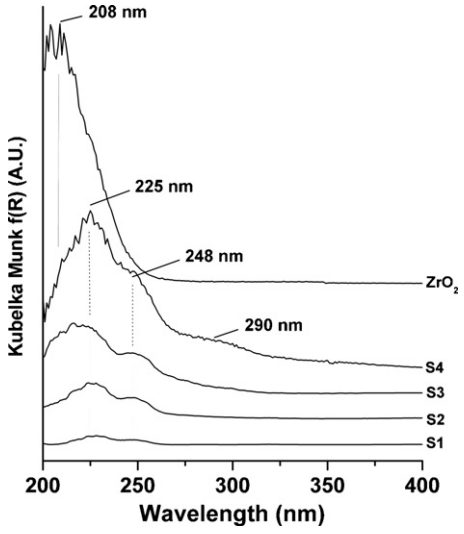

Fig. 4. DR UV–vis spectra of Zr-SBA-15 materials with various Si/Zr molar ratios and commercial ZrO_2.

The above mentioned conclusions are supported by the XPS measurements, in which the different environments of zirconium species supported onto the SBA-15 materials are evaluated, as well as the involvement of the adjacent oxygen species. Figs. 5 and 6 display the XPS spectra recorded for Zr-SBA-15 materials with varying metal contents. Regarding the O1s XPS spectra (Fig. 5) no great differences are clearly distinguishable among the different tested materials. Thus two main oxygen environments are evident in all samples: that corresponding to Si–O bonds (531.9–532.3 eV) and another one centred at 530 eV corresponding to Zr–O–Zr bonds which are attributable to the presence of ZrO_2 domains [40]. However, the latter is more evident in the O1s XPS spectrum recorded from sample S4, suggesting the amount of zirconium dioxide domains are more abundant in this sample than in analogue materials prepared with lower metal contents. Thus, these results are in line with those achieved by DR UV–vis, supporting the conclusions about the presence of Zr–O–Zr species in every tested material and the generation of bulk zirconium dioxide domains in sample S4. The

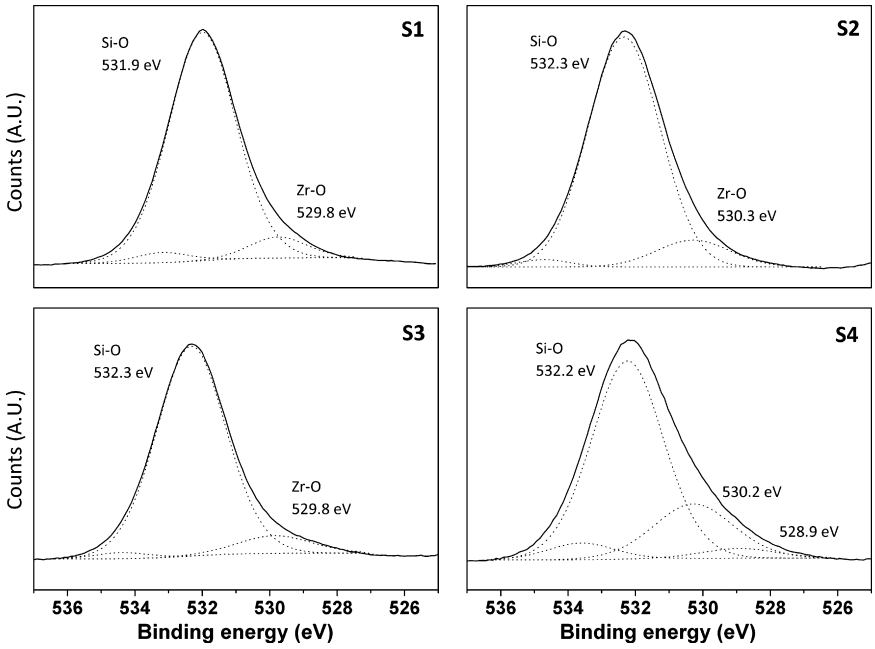

Fig. 5. XPS O1s spectra recorded for Zr-SBA-15 materials showing different zirconium contents.

generation of zirconium dioxide oligomers could be a consequence of the already mentioned incorporation of zirconium species on surface locations. It is noteworthy the formation of Zr–O–Zr occurs even for the material with the lowest metal content (S1), giving another piece of evidence of the incorporation of these species in surface locations [41].

Fig. 6 depicts the XPS Zr3d spectra recorded for the different zirconium-functionalized SBA-15 materials. In this case more complicated spectra are detected, though the differences between the spectra are in agreement with the previous conclusions. Thus, sample S4 displays a Zr3d5/2 line centred at 182.5 eV, indicating the presence of ZrO_2 domains [42], a lower binding energy than that showed by samples S1–S3 (183.0 eV). The lower binding energy found in zirconium sites present in the materials with lower metal contents implies a higher ionicity of the Zr–O bond, involving a higher charge on the Zr cation which is translated into stronger Lewis acid sites in these materials [42], in comparison with zirconium dioxide domains such as those present in sample S4. In this sense, higher acidity, as well as catalytic activity in transesterification reactions, for samples showing lower to medium Zr contents should be expected.

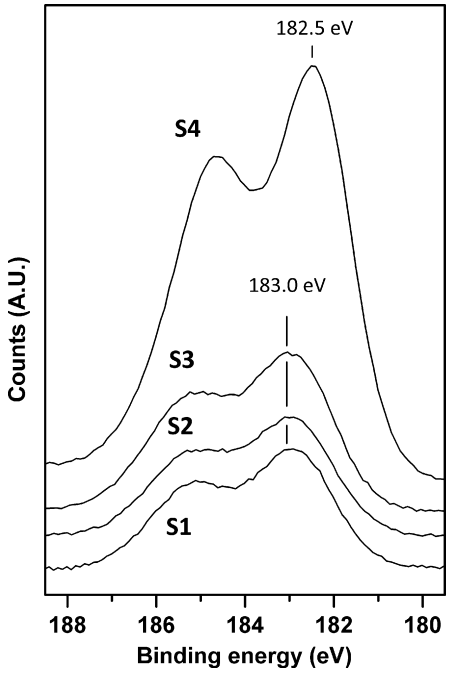

Fig. 6. XPS Zr3d spectra of Zr-SBA-15 materials prepared with various Si/Zr molar ratios.

The NH_3 TPD results included in Table 1 confirm the above-mentioned conclusions. Increasing the zirconium content supported onto the SBA-15-type mesostructured silicas leads to higher population of as well as stronger acid sites. This trend is observed for samples S1–S3 but, as previously stated from XPS results, sample S4 displays much lower acid sites content. Besides, NH_3 TPD profile recorded for this sample evidences a weaker behaviour than that of sample S3. The reasons for these differences are the high dispersion and interaction between the zirconium species supported onto samples S1–S3 in contrast with the bulk ZrO_2 domains observed for sample S4.

3.2. Metal-doped Zr-SBA-15 materials

With the purpose of promoting the acidity of the Zr-SBA-15 materials to be used as catalysts in the transesterification of triglycerides with methanol, sample S3, prepared from a molar ratio Si/Zr = 10 in the synthesis gel was selected as base material to be doped with different metals. This sample has been selected as base material because it contains the highest amount of zirconium species supported onto the silica matrix while preserving good mesoscopic structure with good textural properties. These features combine to lead the highest acid sites loading and strength among the tested Zr-SBA-15 materials. Though there are several possibilities to promote the acidity of zirconium based materials, being sulfation one of the most extended procedure, the demonstration of the very low stability of sulphate ions on zirconium dioxide, especially evident in polar solvents such as the short chain alcohols used in triglyceride transesterification [1], has prompted us to discard this strategy within this work.

Table 2
Physico-chemical properties of metal-doped Zr-SBA-15 materials.

Sample	Doping method	Doping agent	Zr/Me[a]	S_g[b] (m^2/g)	D_p[c] (Å)	V_p[d] (cm^3/g)	Acid loading[e] (meq g^{-1})	T_{max}[f] (°C)
S3	–	–	–	632	106	1.182	0.31	274
S5	Co-condensation	$TiCl_2Cp_2$	159	618	104	1.189	0.19	265
S6		$(NH_4)_6Mo_7O_{24}$	121	596	105	1.135	0.23	294
S7		WCl_6	35	629	104	1.201	0.33	305
S8		WCl_2Cp_2	32	626	100	0.897	0.37	301
S9	Grafting	WCl_6	65	618	106	1.083	0.14	265
S10		WCl_2Cp_2	46	628	105	1.102	0.22	271

[a] Zirconium to doping metal molar ratio in the final sample measured by ICP-AES. Synthesis value Zr/Me = 20.
[b] Surface area measured by the B.E.T. method.
[c] Mean pore size calculated through the B.J.H. method.
[d] Total pore volume recorded at $p/p_0 = 0.985$.
[e] Acid loading measured from NH_3 uptake in TPD profiles.
[f] Maximum of the NH_3-TPD curve.

Two different doping methods were used to combine both kinds of metal precursors, zirconocene dichloride and the doping-metal source. Initially, a direct synthesis procedure was used to prepare the metal-doped Zr-SBA-15 materials, through the joint addition of the different metal sources into the synthesis gel. Since the use of titanium, molybdenum and tungsten have been described to provide increased acidity when doping zirconia-based materials, these metals were used in the acid promotion of sample S3. For this purpose, different metal sources were used, namely: titanocene dichloride, ammonium heptamolybdate, tungsten hexachloride and tungstenocene dichloride. Table 2 lists the physico-chemical properties of the metal-doped Zr-SBA-15 materials. All the samples display good mesoscopic ordering, evaluated through low angle X-ray diffraction (not shown) as well as good textural properties, indicating the addition of the second metal source in the synthesis gel does not cause the destructuration of the material. With regards to the incorporation of the metal species, zirconium loading is close in every case to that achieved for sample S3, used as reference material. On the other hand, great differences were achieved when using the different metal doping agents. Thus, unlike titanium or molybdenum, which are incorporated onto the final material in a very low extent, probably as consequence of the strongly acidic media [32,43], tungsten, either coming from tungsten hexachloride or from tungstenocene dichloride, was incorporated onto the final material in a much higher amount, though none of the samples displayed a total incorporation of the doping metal (synthesis value of Zr/Me = 20).

With the purpose to evaluate the effect of the metal doping on the acidity promotion of the parent Zr-SBA-15 material, NH_3-TPD experiments were carried out. Fig. 7 displays the NH_3-TPD profiles recorded for samples modified with titanium, molybdenum and tungsten, both that prepared from WCl_6 and Cp_2WCl_2, as well as the parent S3 sample. Metal-doped materials do not show a clear promotion of acidity, as both the acid loading and the temperature corresponding to the maximum of the TPD curves are quite similar to those of the non-doped S3 sample. This is probably a consequence of the absence of crystalline phases of zirconium dioxide present in these samples. Thus, tungstated zirconia, taken as example, is known to be a super-acid material because acid sites are formed by the interaction between tungsten oxide onto the surface of crystalline tetragonal zirconia. In our case, the crystallization of zirconium dioxide seems not to occur during the synthesis step, so that the acid sites are not generated. On the contrary, the unexpected acid strength in non-doped Zr-SBA-15 materials could be ascribed to the above mentioned results about the higher ionicity of Zr–O bonds in the SBA-15 supported zirconium-functionalized materials in comparison with bulk oxides. This seems to be related to the strong interaction between the supported zirconium species and the silica support, which enhances the Lewis acidity of the metal sites. Besides, another explanation for this acid strength could be the presence of chlorine atoms interacting with zirconium species which greatly enhances the acid strength of these materials [31]. Chlorine presence was detected by EDS analyses, though the absence of very low binding energy signals in the XPS O1s spectra discards this possibility or at least diminishes the importance of this contribution. On the other hand, the insertion of the second metal functionality does not provide a significant increase on the ammonia desorption temperature for the Me–Zr-SBA-15 materials. In fact, Ti–Zr-SBA-15 as well as Mo–Zr-SBA-15 samples displayed much lower ammonia uptake than its parent zirconium-functionalized material, and also NH_3 desorption was recorded at a lower temperature. Only tungsten provided increased temperature and ammonia uptake with regards to the reference material. These results suggest that the promotion of the acidity of Zr-SBA-15 materials is not effective when using titanium or molybdenum and only slightly effective for tungsten as doping metal. In this latter case, both tungsten hexachloride and tungstenocene dichloride lead to similar acid strength over the final W–Zr-SBA-15 materials, though the latter one seems to provide a higher amount of acid sites, as it is inferred from the larger area below the TPD curve recorded for sample S8. This higher number of acid sites seems to be caused by the nature of the tungsten precursor. As it has previously been described for zirconocene dichloride, the use of the doping agent precursor as a metallocene also leads to the insertion of the metal species inside the micelles, which act as carriers of the metal species for their incorporation onto accessible locations on the mesoporous surface. This is not the case when using tungsten hexachloride, which could dissolve in the synthesis medium

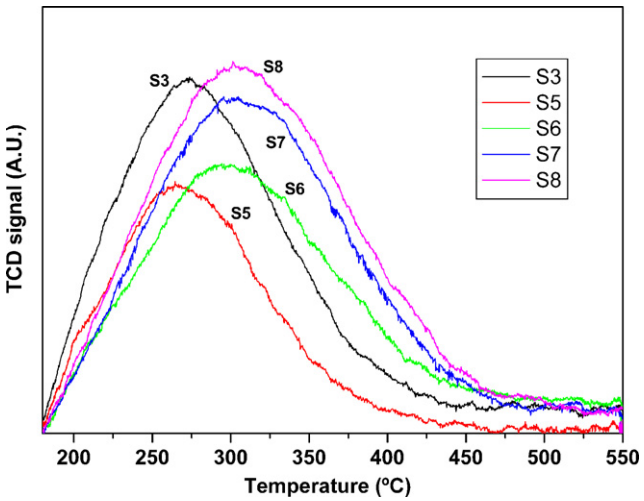

Fig. 7. NH_3-TPD profiles recorded for Zr-SBA-15 and metal-doped Zr-SBA-15 materials prepared from a zirconium to metal ratio of 20 into the synthesis gel.

Table 3
Results from ammonia TPD profiles in W–Zr-SBA-15 materials.

Zr/W[a]	T_{calc}[b] (°C)	Acid loading[c] (mequiv. g^{-1})	T_{max}[d] (°C)	S_g[e] (m^2/g)	V_p[f] (cm^3/g)
1	550	0.21	279	157	0.253
2	550	0.29	281	163	0.295
5	550	0.28	278	641	0.796
10	550	0.30	288	619	0.887
20	550	0.37	301	626	0.897
20	650	0.27	298	602	0.862
20	750	0.23	300	564	0.782
20	850	0.14	301	483	0.628

[a] Zirconium to tungsten molar ratio in the synthesis gel.
[b] Calcination temperature.
[c] Acid loading measured from ammonia uptake.
[d] Maximum of the ammonia desorption curve.
[e] Surface area measured by the B.E.T. method.
[f] Total pore volume recorded at $p/p_0 = 0.985$.

and thus, the accessibility of the metal species is not controlled. In order to determine the effect of a higher accessibility of the doping-metal species, a two-step procedure was used for the preparation of W–Zr-SBA-15 materials. Thus, starting from a Zr-SBA-15 material, prepared with a Si/Zr molar ratio of 10 (Table 1, sample S3), both WCl_6 and Cp_2WCl_2 were thermally grafted onto the surface of the Zr-SBA-15 material, using a starting Zr/W molar ratio of 20 (samples S9 and S10, Table 2). The so-prepared materials displayed TPD profiles with much lower ammonia uptake than their counterparts, prepared through a direct synthesis procedure, suggesting that not only the accessibility of the tungsten sites is important in promoting acidity of Zr-SBA-15 materials but also the nature of the W–Zr species seems to be also crucial. In fact, W–Zr-SBA-15 materials displayed much lower acid loading and strength than that recorded for the parent material, which could be a consequence of the loss of Lewis acidity sites in Zr-SBA-15 materials during the grafting of the tungsten species. For these reasons, the rest of this investigation was carried out using tungstenocene dichloride as doping metal source and by means of a co-condensation procedure to support both zirconium and tungsten sites.

As the most interesting alternative among the different doping metals tested in this work, two different strategies were used in order to enhance the acidity of the tungsten-doped Zr-SBA-15 materials. In a first attempt, the amount of tungsten precursor was increased into the synthesis gel to provide increased number of acid sites over the final materials. A second approach is based on the fact that the tetragonal phase of tungstated zirconia seems to be the main responsible of the acid strength of these materials [44]. The crystallization of zirconium dioxide in tetragonal phase is usually accomplished at high temperatures so that the second strategy for enhancing the acidity of the tungsten–zirconium containing mesostructured materials consisted of the calcination of the starting W–Zr-SBA-15 material (sample S8) at different temperatures.

With regards to the first option, increasing the amount of tungstenocene dichloride into the synthesis gel provided negative results. Table 3 lists the acid loading calculated through ammonia thermal programmed desorption profiles. A reduction of the acid loading was detected as a result of a lower ammonia uptake in-so-far as the amount of tungsten was increased into the synthesis gel. Moreover, the TPD curves were shifted towards lower temperature values when tungsten loading was increased into the synthesis gel, indicating that not only the amount of acid sites diminished but also their acid strength was also lower. The reason for this behaviour probably lays on the reduction of the textural properties observed for these materials. Thus, increasing the amount of tungsten does not lead to an increase of acid loading, but to the reduction of the surface area which makes that lower number of acid sites are readily accessible. Besides, increasing the amount of tungsten into the synthesis gel probably leads to the interaction of adjacent tungsten atoms due to the higher concentration of tungsten in a lower surface area. This leads to a lower dispersion of tungsten, giving weaker acid sites, as ammonia TPD experiments has proved.

Regarding the effect of the calcination temperature, the approach also proved to be uneffective. Thus, increasing the calcination temperature caused, in a similar way to that previously assessed for the effect of the metal loading, the reduction of the acid loading supported onto the mesostructured materials. However, in this case, the strength of the acid sites, estimated from the maximum of the ammonia TPD curve, is rather similar in all of the tested materials. The observed reduction in acid loading should be attributed to the structure shrinking during calcination at high temperatures which lead to lower surface area and pore volume values.

3.3. Catalytic transesterification of crude palm oil with methanol

The assessment of the catalytic activity of Zr-SBA-15 samples and related materials prepared within the present contribution was carried out through the transesterification of crude palm oil (see properties in Table 4) with methanol as short chain alcohols. Based on preliminary experiments, temperature conditions were set at 200 °C, the methanol to oil molar ratio fixed in 30 and the reactions were conducted for 3 h in a stirred batch reactor. Due to the lack of homogeneity of the reaction media, stirring rate was an influential parameter as it strongly affects mass transfer and hence reaction kinetics. Therefore, the highest available stirring rate, 2000 rpm, was chosen. Considering the Zr-SBA-15 materials displayed acid functionality even without the promotion by dop-

Table 4
Properties of crude palm oil used as feedstock for FAME production.

Property	Analysis method	Value
Acid value	ISO 660:96	21.4 mg KOH/g
Water content	UNE-EN-ISO 662:01 Met.B	0.068 wt.%
Rubber (P)	UNE 55.108-73	22.0 ppm
Iodine index	ISO 3961:00	50
Density (20 °C)	ISO 6883:00	928 Kg m^{-3}
Stability against oxidation (AOM-97.8 °C)	ISO 6886:96	19.5 h
Fatty acid profile	ISO 5508:90/ISO 5509:00	Weight %
	Lauric acid (12:0)	0.16
	Myristic acid (14:0)	0.99
	Palmitic acid (16:0)	43.03
	Palmitoleic acid (16:1)	0.19
	Stearic acid (18:0)	4.31
	Oleic acid (18:1)	39.47
	Linoleic acid (18:2)	10.82
	Linolenic acid (18:3)	0.29

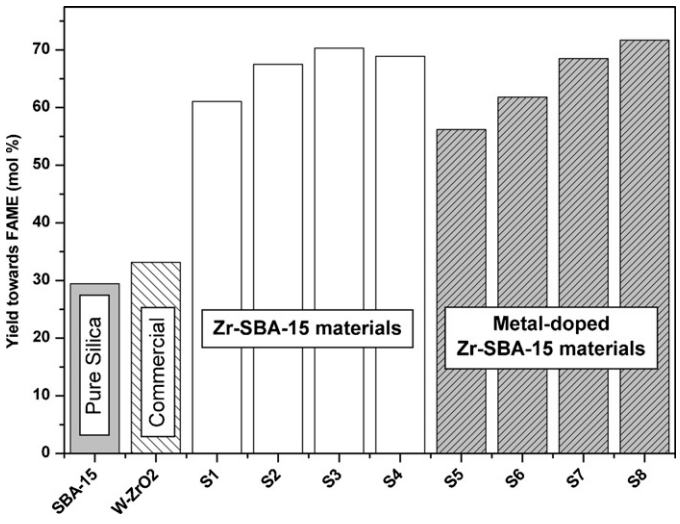

Fig. 8. Reaction results for FAME production using Zr-SBA-15 and metal-doped related materials as catalysts. Reference runs have been accomplished in presence of pure silica SBA-15 and commercial tungstated zirconia. Reaction conditions: 200 °C; methanol:oil molar ratio = 30; catalyst loading 10 wt.%; time 3 h; stirring rate 2000 rpm.

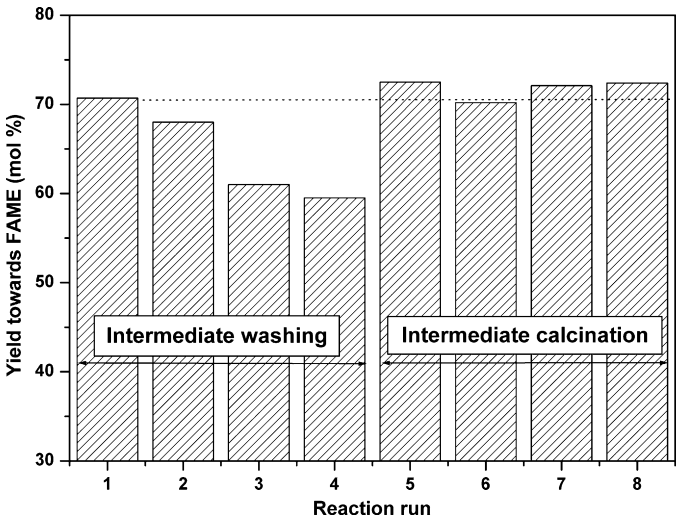

Fig. 9. Recycling catalytic tests for Zr-SBA-15 sample S3. Reaction conditions: 200 °C; methanol:oil molar ratio = 30; catalyst loading 10 wt.%; time 3 h; stirring rate 2000 rpm.

ing metals, several catalytic runs were carried out using Zr-SBA-15 materials showing different metal loadings. Also, the samples prepared through metal doping were assayed in the reaction. Fig. 8 displays the catalytic activity showed by Zr-SBA-15 materials with different zirconium loadings as well as by metal-doped Zr-SBA-15 samples, prepared from different metal precursors. Finally, two reaction runs were also performed for reference purposes using a pure silica SBA-15 material and a commercial tungstated zirconia (MEL chemicals, 300 $m^2\ g^{-1}$) as catalyst. From reaction results it is noteworthy the outstanding catalytic activity Zr-SBA-15 materials display without the needing to promote its acid strength by any doping metal. Thus, materials S1–S4 provided yields to FAME over 60%, which is twice that recorded in presence of the pure silica-SBA-15 material (29.3%). At this point it is important to note that the observed FAME yield in this blank reaction is not due to the catalytic activity of a pure silica SBA-15 material but to the presence of FFA in the starting oil feedstock (see Table 4), which catalyzes the transesterification reactions, an observed trend previously reported for similar feedstocks [45].

Silicon to zirconium ratio in Zr-SBA-15 materials also seems to have an impact on the catalytic activity of the same. Thus, sample S3 (Si/Zr synthesis value of 10) appears as the most active sample within the series giving 72% FAME yield. Higher and lower Si/Zr molar ratios provided slightly lower activity. The reason is sample S3 is prepared with the highest metal loading showing no bulk zirconium dioxide, and thus, the acid loading and acid strength of the supported oligomerized zirconium species is maximum for this material, among the tested samples, accordingly to the NH_3 TPD experiments.

Nevertheless, the catalytic activity of these Zr-SBA-15 materials contrasts with that showed by the commercial tungstated zirconia-based catalyst used for comparison purposes, which provides 33% yield to FAME. This higher catalytic activity in Zr-SBA-15 materials could be related to the above mentioned stronger acidic Lewis sites detected by means of XPS, because of the interaction between zirconium species and the silica support.

On the other hand, and as a negative fact, the insertion of the different doping metals into the synthesis gel of the Zr-SBA-15 materials does not provide the expected increasing in the catalytic activity, bearing in mind the enhancement produced in the acid strength and loading when using tungsten as doping metal. Thus, both titanium and molybdenum lead samples which displayed a much lower catalytic activity than the Zr-SBA-15 parent material whereas tungsten provided similar catalytic activity to sample S3. In this way, though the acidity of Zr-SBA-15 samples is enhanced by tungsten, it seems this fact is not enough for the promotion of the catalytic activity of Zr-SBA-15 materials for FAME production by triglyceride transesterification. Some explanation for this behaviour could lay on the increasing of the metal loading, making more plausible the formation of bulk metal oxide domains, showing a lower interface area, and thus, much lower surface acid groups. Thus, increasing the amount of metal loading above metal to silicon molar ratio of 10 seems to be negative for the catalytic purposes.

In order to determine the stability of Zr-SBA-15 materials in FAME production from crude palm oil, several recycling tests were carried out. Fig. 9 displays the reaction results achieved from recycling tests which were carried out in presence of sample S3 as catalyst. The first four runs were performed with intermediate washing [34] for the removal of adsorbed polar compounds which have been proposed to be the responsible for the catalytic activity decay detected in this kind of reaction cycles [46]. However, the washing procedure is not completely efficient as there is a gradual loss of activity after each run (from 72% FAME to 60% FAME yield in the fourth run) and thus, regeneration of the initial catalytic activity is not complete. On the other hand, following a thermal procedure for catalyst regeneration (consisting on a calcination step in air atmosphere at 550 °C during 5 h), the starting activity of Zr-SBA-15 material was fully recovered. Furthermore, the complete regeneration was confirmed and maintained for 4 additional reaction runs carried out with intermediate calcination. These results confirm the excellent stability and regenerability of Zr-SBA-15 materials in FAME production by transesterification of crude palm oil with methanol.

4. Conclusions

The use of zirconocene dichloride as metal precursor for the synthesis of Zr-SBA-15 materials allows preparing zirconium functionalized materials with a high amount of metal loading while preserving the high mesoscopic ordering typical from SBA-15 materials. The so-prepared samples display acid properties, which could be related to the presence of strong Lewis acid sites formed by supporting the zirconium species onto the surface of SBA-15 materials. These materials have revealed to present excellent catalytic

activity in the transesterification of crude palm oil with methanol, in which highly acid functionality is needed. The use of secondary transition metals as doping agents for promoting the acid properties of Zr-SBA-15 materials, such as titanium, molybdenum and tungsten, did not provide significant enhancements. Only tungsten allowed a slight improvement of the acid properties of the Zr-SBA-15 materials, but this is not translated into a higher catalytic activity in the transesterification of palm oil. Finally, Zr-SBA-15 materials displayed excellent stability and reusability, being recyclable for at least eight consecutive reaction runs in FAME production from crude palm oil with methanol with intermediate calcination at 550 °C.

Acknowledgements

The financial support from the Spanish Science and Innovation Ministry through the project CTQ2008-01396 and from the Regional Government of Madrid through the project S2009-ENE1743 is gratefully acknowledged. The Spanish government is kindly acknowledged by the award of a FPI grant (R.S.-V.). The authors wish to thank Dr. R. Luque for the access to XPS measurements and valuable discussions (Department of Organic Chemistry, Universidad de Córdoba).

References

[1] J.A. Melero, J. Iglesias, G. Morales, Green Chem. 11 (2009) 1285–1308.
[2] F.R. Ma, M.A. Hanna, Bioresour. Technol. 70 (1999) 1–15.
[3] A. Behr, A. Westfechtel, J. Pérez Gomes, Chem. Eng. Technol. 31 (2008) 700–714.
[4] J.A. Duffield, Inhal. Toxicol. 19 (2007) 1029–1031.
[5] F. Ma, L.D. Clements, M.A. Hanna, Trans ASAE 41 (1998) 1261–1264.
[6] P.T. Vasudevan, M. Briggs, J. Ind. Microbiol. Biotechnol. 35 (2008) 421–430.
[7] A. Behr, J. Pérez Gomes, Eur. J. Lipid Sci. Technol. 112 (2010) 31–50.
[8] J.M. Marchetti, V.U. Miguel, A.F. Errazu, Fuel Process. Technol. 89 (2008) 740–748.
[9] E. Lotero, Y. Liu, D.E. Lopez, K. Suwannakarn, D.A. Bruce, J.G. Goodwin Jr., Ind. Eng. Chem. Res. 44 (2005) 5353–5363.
[10] A. Demirbas, Energy Convers. Manage. 49 (2008) 125–130.
[11] K. Arata, Green Chem. 11 (2009) 1719–1728.
[12] B.M. Reddy, M.K. Patil, Chem. Rev. 109 (2009) 2185–2208.
[13] B.M. Reddy, M.K. Patil, Curr. Org. Chem. 12 (2008) 118–140.
[14] S. Ramu, N. Lingaiah, B.L.A. Prabhavathi Devi, R.B.N. Prasad, I. Suryanarayana, P.S. Sai Prasad, Appl. Catal. A 276 (2004) 163–168.
[15] A.A. Kiss, A.C. Dimian, G. Rothenberg, Adv. Synth. Catal. 348 (2006) 75–81.
[16] K. Suwannakarn, E. Lotero, K. Ngaosuwan, J.G. Goodwin Jr, Ind. Eng. Chem. Res. 48 (2009) 2810–2818.
[17] B. Fu, L. Gao, L. Niu, R. Wei, G. Xiao, Energy Fuels 23 (2009) 569–572.
[18] S. Furuta, H. Matsuhashi, K. Arata, Catal. Commun. 5 (2004) 721–723.
[19] K. Ngaosuwan, X. Mo, J.G. Goodwin Jr., P. Praserthdam, Appl. Catal. A 380 (2010) 81–86.
[20] J. Jitputti, B. Kitiyanan, P. Rangsunvigit, K. Bunyakiat, L. Attanatho, P. Jenvanitpanjakul, Chem. Eng. J. 116 (2006) 61–66.
[21] S. Martins Garcia, L. Teixeira, U. Ledo Marciniuk, Schuchardt, Bioresour. Technol. 99 (2008) 6608–6613.
[22] E. Ghedini, M. Signoretto, F. Pinna, Catal. Lett. 125 (2008) 359–370.
[23] F.-S. Xiao, Top. Catal. 35 (2005) 9–23.
[24] L. Fuxiang, Y. Feng, L. Yongli, L. Ruifeng, X. Kechang, Microporous Mesoporous Mater. 101 (2007) 250–255.
[25] Y. Du, S. Liu, Y. Zhang, F. Nawaz, Y. Ji, F.-S. Xiao, Micropor. Mesopor. Mater. 121 (2009) 185–193.
[26] X.-Q. Zhang, S.-J. Wang, J.-W. Wang, L.-L. Lou, C. Zhang, X. Liu, Solid State Sci. 11 (2009) 1412–1418.
[27] I. Jiménez-Morales, J. Santamaría-González, P. Maireles-Torres, A. Jiménez-López, Appl. Catal. A 379 (2010) 61–68.
[28] M.S. Wong, H.C. Huang, J.Y. Ying, Chem. Mater. 14 (2002) 1961–1973.
[29] X.-X. Wang, F. Lefebvre, J. Patarin, J.-M. Basset, Microporous Mesoporous Mater. 42 (2001) 269–276.
[30] X.-X. Wang, L. Veyre, F. Lefebvre, J. Patarin, J.-M. Basset, Microporous Mesoporous Mater. 66 (2003) 169–179.
[31] M.D. Gracia, A.M. Balu, J.M. Campelo, R. Luque, J.M. Marinas, A.A. Romero, Appl. Catal. A 371 (2009) 85–91.
[32] J.A. Melero, J.M. Arsuaga, P. de Frutos, J. Iglesias, J. Sainz, S. Blázquez, Microporous Mesoporous Mater. 86 (2005) 364–373.
[33] R. van Grieken, G. Calleja, G.D. Stucky, J.A. Melero, R.A. García, J. Iglesias, Langmuir 19 (2003) 3966–3973.
[34] K. Jacobson, R. Gopinath, L.C. Meher, A.K. Dalai, Appl. Catal. B 85 (2008) 86–91.
[35] G. Gelbard, O. Brès, R.M. Vargas, F. Vielfaure, U.F. Schuchardt, J. Am. Oil Chem. Soc. 72 (1995) 1239–1241.
[36] M.E. Raimondi, L. Marchese, E. Gianotti, T. Maschmeyer, J.M. Seddon, S. Coluccia, Chem. Commun. 1 (1999) 87–88.
[37] K.S.W. Sing, D.H. Everett, R.A.W. Haul, L. Moscou, R.A. Pierotti, J. Rouquerol, T. Siemieniewska, Pure Appl. Chem. 57 (1984) 603–619.
[38] C.K. Krishnan, T. Hayashi, M. Ogura, Adv. Mater. 20 (2008) 2131–2136.
[39] S.-Y. Chen, J.-F. Lee, S. Cheng, J. Catal. 270 (2010) 196–205.
[40] S. Damyanova, P. Granges, B. Delmon, J. Catal. 168 (1997) 421–430.
[41] J.-M. Liu, S.-J. Liao, G.-D. Jiang, X.-L. Zhang, L. Petrik, Microporous Mesoporous Mater. 95 (2006) 306.
[42] H.J.M. Bosman, A.P. Pijpers, A.W.M.A. Jaspers, J. Catal. 161 (1996) 551–559.
[43] J.A. Melero, J. Iglesias, J.M. Arsuaga, J. Sainz-Pardo, P. de Frutos, S. Blázquez, Appl. Catal. A 331 (2007) 84–94.
[44] X.-R. Chen, Y.-H. Ju, C.-Y. Mou, J. Phys. Chem. C 111 (2007) 18731–18737.
[45] S.A. Pasias, N.K. Barakos, N.G. Papayannakos, Ind. Eng. Chem. Res. 48 (2009) 4266–4273.
[46] A.C. Alba-Rubio, F. Vila, D. Martín Alonso, M. Ojeda, R. Mariscal, M. López Granados, Appl. Catal. B 95 (2010) 279–287.